Role of Maritime Continent Land Convection on the Mean State and MJO Propagation

MIN-SEOP AHN

Department of Atmospheric Sciences, University of Washington, Seattle, Washington, and Department of Oceanography, Chonnam National University, Gwangju, South Korea

DAEHYUN KIM

Department of Atmospheric Sciences, University of Washington, Seattle, Washington

YOO-GEUN HAM

Department of Oceanography, Chonnam National University, Gwangju, South Korea

SUNGSU PARK

School of Earth and Environmental Sciences, Seoul National University, Seoul, South Korea

(Manuscript received 13 May 2019, in final form 7 November 2019)

ABSTRACT

The Maritime Continent (MC) region is known as a ''barrier'' in the life cycle of the Madden–Julian oscillation (MJO). During boreal winter, the MJO detours the equatorial MC land region southward and propagates through the oceanic region. Also, about half of the MJO events that initiate over the Indian Ocean cease around the MC. The mechanism through which the MC affects MJO propagation, however, has remained unanswered. The current study investigates the MJO–MC interaction with a particular focus on the role of MC land convection. Using a global climate model that simulates both mean climate and MJO realistically, we performed two sensitivity experiments in which updraft plume radius is set to its maximum and minimum value only in the MC land grid points, making convective top deeper and shallower, respectively. Our results show that MC land convection plays a key role in shaping the 3D climatological moisture distribution around the MC through its local and nonlocal effects. Shallower and weaker MC land convection results in a steepening of the vertical and meridional mean moisture gradient over the MC region. The opposite is the case when MC land convection becomes deeper and stronger. The MJO's eastward propagation is enhanced (suppressed) with the steeper (lower) mean moisture gradient. The moist static energy (MSE) budget of the MJO reveals the vertical and meridional advection of the mean MSE by MJO wind anomalies as the key processes that are responsible for the changes in MJO propagation characteristics. Our results pinpoint the critical role of the background moisture gradient on MJO propagation.

1. Introduction

The Madden–Julian oscillation (MJO; Madden and Julian 1971, 1972) is the dominant mode of intraseasonal (30–90 days) variability in the tropics. The MJO is essentially a planetary-scale (zonal wavenumber 1–3), eastward-propagating (phase speed of $\sim 5\,\mathrm{m\,s^{-1}}$ over the Indo-Pacific warm pool) envelope of anomalous convective activity coupled with large-scale circulation (Zhang 2005). The MJO influences a wide range of weather and climate phenomena globally (Zhang 2013) and thereby provides a major source of predictability in the intraseasonal time scale (Lau and Waliser 2012).

The observed eastward propagation of the MJO over the Maritime Continent (MC) exhibits two features that are distinct from that over the open oceans. First, the center of the MJO's convective envelope tends to ''detour'' the equatorial MC islands southward and moves through the oceanic region between Indonesia and Australia in boreal winter (e.g., Wang and Rui 1990; Wu and Hsu 2009; Kim et al. 2017; Zhang and Ling 2017).

Corresponding authors: Daehyun Kim, daehyun@uw.edu; Sungsu Park, sungsup@snu.ac.kr

DOI: 10.1175/JCLI-D-19-0342.1

Second, MJO propagation is often interrupted in the MC region (e.g., Kim et al. 2014; Feng et al. 2015; Zhang and Ling 2017; Stachnik et al. 2015; DeMott et al. 2018), a feature that is known as the "MC barrier effect." In particular, Zhang and Ling (2017) showed that about a half of the MJO events that initiate over the Indian Ocean cease over the MC. While these characteristics of the MJO in the MC region have been well documented, our understanding of the underlying mechanism is still limited [see the review of Kim et al. (2020)].

Previous studies have emphasized the topography in the MC islands and the land–sea contrast within the MC region as key factors that are responsible for the two peculiar behaviors of the MJO mentioned above. For example, Hsu and Lee (2005) and Wu and Hsu (2009) suggested that the steep MC topography disturbs the MJO perturbation wind, causing the MJO to weaken over the MC area. Sobel et al. (2010) proposed a mechanism that is based on the argument that the surface latent heat flux is critical to MJO maintenance. That is, the MJO weakens over the MC area because moisture supply to the MJO via surface latent heat flux is limited there, especially over the landmasses (i.e., MC islands), where surface heat capacity is too small to sustain intraseasonal heat flux anomalies.

If either the topography or the land–sea contrast is the main cause of the MC barrier effects and MJO detouring, the full-geography models should able to realistically capture the observed characteristics of the MJO in the MC region. However, many contemporary GCMs tend to exaggerate the MC barrier effect, overestimating the probability of an MJO event being terminated over the MC region (Kim et al. 2009; Hung et al. 2013; Jiang et al. 2015; Ahn et al. 2017; Ling et al. 2017). In addition, in some models, MJO forecast skill is limited mainly due to the deficiency in MJO-related convection over the MC (Vitart et al. 2007; Seo et al. 2009; Kim et al. 2016, 2018). The stronger-than-observed MC barrier effects in the models indicate that there might be some mechanism that is not fully simulated in the models through which the MC islands affect the MJO.

Motivated by the fact that the MC region hosts a strong, persistent diurnal cycle of precipitation, especially on and near the islands, other studies focused on the role of the diurnal cycle of convection (Peatman et al. 2014; Hagos et al. 2016; Zhang and Ling 2017; Ling et al. 2019). Using a cloud-permitting regional model, Hagos et al. (2016) showed that MJO propagation over the MC is enhanced in the simulation of an MJO episode when the diurnal cycle of MC land convection is weakened. They suggested that a stronger diurnal cycle of convection results in overall a stronger MC land convection, and the enhanced MC land convection could weaken the oceanic convection by enhancing land–sea breezes and limiting moisture supply to the oceanic area. Citing that MJO-associated convection is mostly over water, they further hypothesized that the occasional disruption of MJO propagation over the MC ocean is the result of the competition between land and oceanic convection. Zhang and Ling (2017) found that the MJO events that initiate over the Indian Ocean and terminate over the MC ("blocked" MJO events in their terminology) are associated with a higher land-to-ocean precipitation ratio than in the MJO events that propagate through the MC, supporting the land versus ocean competition idea. Ling et al. (2019) further suggested that soil moisture can affect the strength of MC land convection, hence the land versus ocean competition.

Meanwhile, inspired by the recent theoretical development that explains propagation and maintenance of the MJO by those of moisture anomalies (moisture mode theory; Adames and Kim 2016; Sobel and Maloney 2012, 2013; Raymond and Fuchs 2009; Fuchs and Raymond 2017), many recent studies examined the moisture or moist static energy (MSE) budget of the MJO in observations and model simulations, providing new insights into the role of the basic state, especially that of lower free-tropospheric humidity. Gonzalez and Jiang (2017) found a systematic difference between a good-MJO model group and a poor-MJO model group in the amount of lower free-tropospheric humidity over the MC region; in the good-MJO models, the MC area is systematically wetter in the lower troposphere than in the poor-MJO models, which is associated with a much steeper meridional and vertical gradient of the climatological mean moisture. Using the same model set, Wang et al. (2017) suggested that the steeper meridional and vertical gradient of the mean moisture are responsible for increasing meridional and vertical advection of mean MSE by intraseasonal wind in good-MJO models. Jiang (2017) further showed that the steeper meridional moisture gradient enhances meridional moisture advection, the key moisture budget term for MJO propagation over the MC region (Kim et al. 2014, 2017; Jiang 2017; Wang et al. 2017), explaining the better skill of the good-MJO models in representing the MJO's eastward propagation. With an MSE budget analysis of the observed MJO, Kim et al. (2017) suggested that the anomalous moisture and convection associated with the MJO detour the equatorial MC area partly because the mean horizontal moisture gradient is weaker there than in the oceanic region between Indonesia and Australia.

Despite the critical role of the mean state moisture distribution on MJO propagation highlighted in many recent studies, our understanding of the factors that determine the seasonal mean moisture pattern around the MC region is limited. Based on a very limited

amount of observations available in his time, Ramage (1968) argued that the MC is "the greatest source of energy for the extratropical circulation." Since then, studies have suggested that convection in the MC region plays an important role in modulating the mean state around the MC. Neale and Slingo (2003) performed a set of two simulations using a GCM; one with realistic MC geography and another with MC islands being replaced by open ocean. They found significant changes in the distribution of the mean rain rate around the MC region. Interestingly, the mean state rain-rate distribution was more realistic with a reduced dry bias in the simulation without the MC islands. Tseng et al. (2017) conducted a similar set of simulations and also found that the basic state varies significantly when either the topography or all landmasses are removed in the MC region.

The results of the modeling studies mentioned above strongly suggest that the topography, land–sea mask, and convection in the MC area are interacting with the large-scale circulation—such as the local Hadley and Walker circulations—to determine the mean state. The nature of convection in the MC islands is tightly linked to the topography and land–sea contrast, as those geographical factors are known to play critical role in the diurnal cycle of convection in and around the MC islands (Neale and Slingo 2003). Therefore, if, for example, the MC islands are removed in a model simulation, both the boundary condition and the characteristics of convection change, meaning it is not easy to disentangle the effect of one from that of another. In other words, it would be difficult, if not impossible, to isolate the role of convection itself from those of landmasses.

In this study, we focus on the role of convection in the MC islands on the basic state and MJO propagation. In an attempt to isolate the role of convection from that of the surface boundary condition–land–sea mask and topography, we configured idealized GCM experiments, in which convection over the MC islands is perturbed to be either deeper or shallower. It will be shown that both the basic state and MJO propagation characteristics are heavily affected by the changes in MC land convection.

This paper is organized as follows. The model, the experimental design, the diagnostics used in this study, and the validation dataset are described in section 2. The analysis results are presented in section 3. A summary and discussion are given in section 4.

2. Data and method

a. Model and experimental design

The general circulation model (GCM) used in our study is the Seoul National University Atmosphere Model version 0 with a Unified Convection Scheme (SAM0-UNICON; Park et al. 2019), which is a new atmospheric GCM based on the Community Atmosphere Model version 5 (CAM5; Neale et al. 2012; Park et al. 2014) wherein UNICON (Park 2014a,b) replaces CAM5's shallow (Park and Bretherton 2009) and deep convection schemes (Zhang and McFarlane 1995) and a revised treatment of the convective detrainment process (Park et al. 2017). SAM0-UNICON is one of the GCMs that participated in the sixth coupled model intercomparison project (CMIP6; Eyring et al. 2016). Park et al. (2019) compared the simulation of SAM0-UNICON to that of CAM5 with same configurations of model time steps and resolution (1.25° longitude × 0.95° latitude with 30 vertical layers). It was shown that the global mean climate and El Niño–Southern Oscillation simulated by SAM0-UNICON is roughly similar to those of CAM5 but SAM0-UNICON substantially improves the simulations of the MJO, diurnal cycle of precipitation, tropical cyclones, aerosol indirect effects, and atmospheric teleconnection associated with the MJO (Yoo et al. 2015; Ahn et al. 2019; Park et al. 2019).

We first ran SAM0-UNICON for 20 years by prescribing the observed climatological seasonal cycle of sea surface temperature and sea ice concentration. This simulation, which was made with default configurations, will be referred to as the control simulation (Control) hereafter. In UNICON, there are constants that set the minimum (for nonorganized state) and maximum (for maximally organized state) updraft plume radius over the ocean and land areas. The control simulation uses the updraft plume radius over land of 100 and 9000 m for the minimum and maximum updraft plume radius, respectively. In addition to the control simulation, we configured two idealized experiments, in which land convection over the MC is perturbed to be shallower and weaker ($R_{\min}$) and deeper and stronger ($R_{\max}$). The land updraft plume radius over the MC is set to 100 m for $R_{\min}$ and to 9000 m for $R_{\max}$. The updraft plume radius effectively controls convective top height by modulating lateral entrainment rate. Updraft plumes with smaller radius could easily be diluted by lateral entrainment of environmental air, which is drier than that of the updraft plumes, while those with larger radius could grow deeper due to smaller dilution by entrainment. The entrainment rate is parameterized as an inverse function of the convective updraft plume radius with additional consideration of evaporative enhancement factor in UNICON. Figures 1a–c show the mean cumulus top height for boreal winter. Compared to Control, the cumulus top height over the MC land region is overall lower in $R_{\min}$, and higher in $R_{\max}$. This indicates that changing the maximum and minimum updraft plume

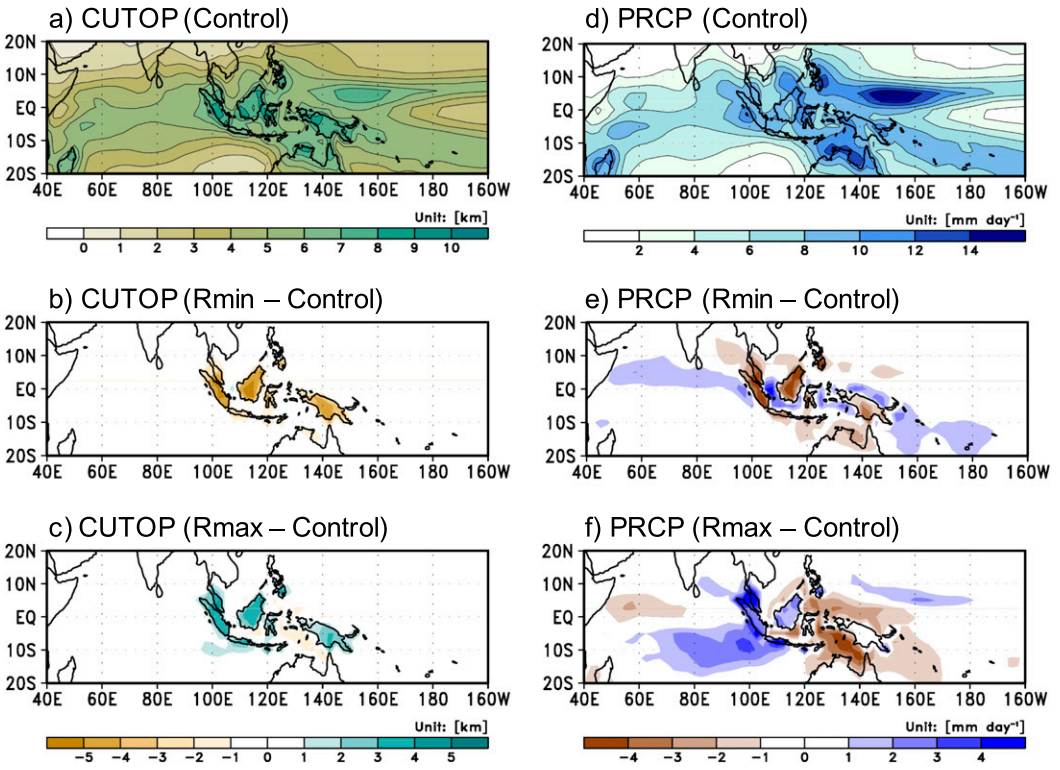

FIG. 1. Horizontal patterns of boreal winter (November–April) mean (a)–(c) cumulus top height (km) and (d)–(f) precipitation (mm day^{-1}): (top) Control, (middle) $R_{\min}$ minus Control, and (bottom) $R_{\max}$ minus Control.

radius is an effective way of altering cumulus activity. All simulations were performed at 2.5° longitude and 1.9° latitude horizontal resolutions with 30 vertical levels. The simulated model output is interpolated into 2.5° longitude and 2.5° latitude horizontal grids for analysis. Our analysis focuses on boreal winter (November–April) when the MJO variability is most pronounced.

b. *Analysis method*

To examine MJO propagation, we use the lag–longitude diagrams that are based on lead–lag regressions of intraseasonal (i.e., 20–100-day bandpass filtered) precipitation against its area-averaged time series over the Indian Ocean (i.e., 5°S–5°N, 85°–95°E). The lag–longitude diagram is designed to capture characteristics of the MJO's eastward propagation, including the zonal extent of the propagation range, and the propagation speed. This diagnostic has been used in many MJO studies (e.g., Waliser et al. 2009; Kim et al. 2009; Jiang et al. 2015).

The MSE budget analysis has been used for examining MJO propagation and maintenance mechanisms in many MJO studies (e.g., Maloney 2009; Kiranmayi and Maloney 2011; Andersen and Kuang 2012; Kim et al. 2014; Arnold et al. 2015; Jiang 2017; Wang et al. 2017). The vertically integrated MSE equation has the following form:

$$\left\langle \frac{\partial h}{\partial t} \right\rangle' = -\left\langle u\frac{\partial h}{\partial x} \right\rangle' - \left\langle v\frac{\partial h}{\partial y} \right\rangle' - \left\langle \omega\frac{\partial h}{\partial p} \right\rangle' + \langle \mathrm{LW} \rangle' + \langle \mathrm{SW} \rangle' + \langle \mathrm{LHF} \rangle' + \langle \mathrm{SHF} \rangle', \quad (1)$$

where h is MSE ($h = CpT + gz + Lq$); u, v, ω are zonal, meridional, vertical pressure velocity, respectively; LW and SW are longwave and shortwave radiation; and LHF and SHF are surface latent heat flux and surface sensible heat flux. The angle bracket indicates a mass-weighted vertical integral from the surface to 100 hPa and the prime denotes intraseasonal anomalies. In Eq. (1), to obtain intraseasonal anomalies, a 20–100-day bandpass filter is applied to individual MSE budget terms. Following Andersen and Kuang (2012), we directly calculate the MSE tendency by backward time differentiation of $\langle h \rangle$ and obtain the corresponding residual term by subtracting the sum of MSE budget terms on the rhs of Eq. (1) from the directly calculated MSE tendency.

In section 3b, the meridional and vertical MSE advection terms in Eq. (1) are further decomposed to examine relative roles of the changes in the mean state and

in the MJO circulation. The MSE and velocity are decomposed into low-frequency mean state (>100 days), intraseasonal (20–100 days), and high-frequency (<20 days) components. For example, h can be decomposed as

$$h = \overline{h} + h' + h'' + \varepsilon,$$

where the overbar, prime, and double prime indicate 101-day running mean, 20–100-day bandpass filtered anomaly, and 20-day high-pass filtered anomaly, respectively. The filtering is performed after removing the 101-day running mean from the total field. ε indicates the residual caused by filtering truncation. Here ε is negligible and does not affect the results (not shown). With this decomposition, the advection terms can be decomposed into nine terms. Among the nine terms, we show in the result section only three terms—the mean MSE advection by intraseasonal wind, the intraseasonal MSE advection by mean wind, and the high-frequency MSE advection by high-frequency wind—that have considerable magnitude. Therefore, for the meridional advection term, the result of the decomposition reads as follows:

$$\left\langle v\frac{\partial h}{\partial y}\right\rangle' \approx \left\langle v'\frac{\partial \overline{h}}{\partial y}\right\rangle' + \left\langle \overline{v}\frac{\partial h'}{\partial y}\right\rangle' + \left\langle v''\frac{\partial h''}{\partial y}\right\rangle', \quad (2)$$

where all the notations have the same definitions with those described above. The vertical advection term is decomposed in the same manner.

To examine the role of each MSE budget term on MJO propagation over the MC, we first regress each MSE budget term onto intraseasonal precipitation averaged over the Indian Ocean, and then show the area and lag-day-averaged values of them (e.g., Fig. 9). Note that this method is different from the method based on normalized covariances of individual MSE budget terms with MSE anomaly or MSE tendency (e.g., Andersen and Kuang 2012; Arnold et al. 2013; Jiang 2017; Adames et al. 2017), which is more suitable for examining global propagation and our method is for focusing on regional propagation over the MC.

c. Validation dataset

Daily averaged precipitation from the Tropical Rainfall Measuring Mission 3B42 version 7 (TRMM 3B42v7; Huffman et al. 2007) product and daily averaged temperature, specific humidity, and geopotential height from the European Centre for Medium-Range Weather Forecasts (ECMWF) interim reanalysis (ERA-Interim; Dee et al. 2011) are used as the reference values. The data are obtained for the period of 1998–2015 and interpolated into 2.5° longitude and 2.5° latitude horizontal grids.

3. Result

a. Effects of MC land convection on the mean state

We begin by examining the mean state changes associated with the modifications made in the maximum (R_{min}) and minimum (R_{max}) convective plume radius over the MC landmasses. The focus of the analysis presented in this subsection is on the horizontal and vertical moisture gradient of the mean moisture, which have been suggested to be key aspects of the mean state in regard to the propagation of the MJO in observations (e.g., Adames et al. 2016; Kim et al. 2017; Jiang et al. 2018) and in model simulations (Jiang 2017; Gonzalez and Jiang 2017; Wang et al. 2017).

Figures 1d–f show the spatial pattern of the mean precipitation in Control, and the difference of R_{min} and R_{max} from Control. In R_{min}, the mean precipitation decreases over the MC islands and increases over the surrounding ocean areas. In contrast, R_{max} shows increased land precipitation, except over New Guinea island, with decreased ocean precipitation, in particular to the east of 110°E. Overall, the oceanic precipitation increases when land convection is suppressed and vice versa, except over the ocean area to the west of 110°E and between the equator and 20°S. Because our modifications in the convection scheme directly affect only MC land convection, the systematic changes in ocean precipitation in Figs. 1e and 1f suggest that there may be a connection between land and ocean convection over the MC, supporting the "competition" idea proposed in previous studies (Hagos et al. 2016; Zhang and Ling 2017).

Figure 2 shows model-simulated temperature tendency by moist processes ($Q1_c$) and vertical pressure velocity (ω) averaged over the land (orange), ocean (blue), and all (gray) grid points in the western MC area (5°S–5°N, 100°–120°E). $Q1_c$ consists of the temperature tendency produced by cloud physics and convective process. In Control, a strong positive $Q1_c$ and associated mean upward motion appear (Figs. 2a,d). In R_{min}, with the overall decrease in the mean cumulus top height (Fig. 1b), $Q1_c$ is much weaker (slightly stronger) above (below) 700 hPa than that in Control (Fig. 2b). Consistent changes in the mean vertical motion are also observed; a large reduction in the mean upper-level upward motion and increase in the lower-level mean vertical velocity (Fig. 2e).

The R_{max} exhibits similar amplitude changes in the mean $Q1_c$ and ω but with the opposite sign. The mean $Q1_c$ increases in the upper-level over the land MC area because deep convection is enhanced (Fig. 1c) and the enhanced heating over land MC area yields the mean upward motion in the upper level that is stronger than those in Control (Fig. 2f). In both R_{min} and R_{max}, the

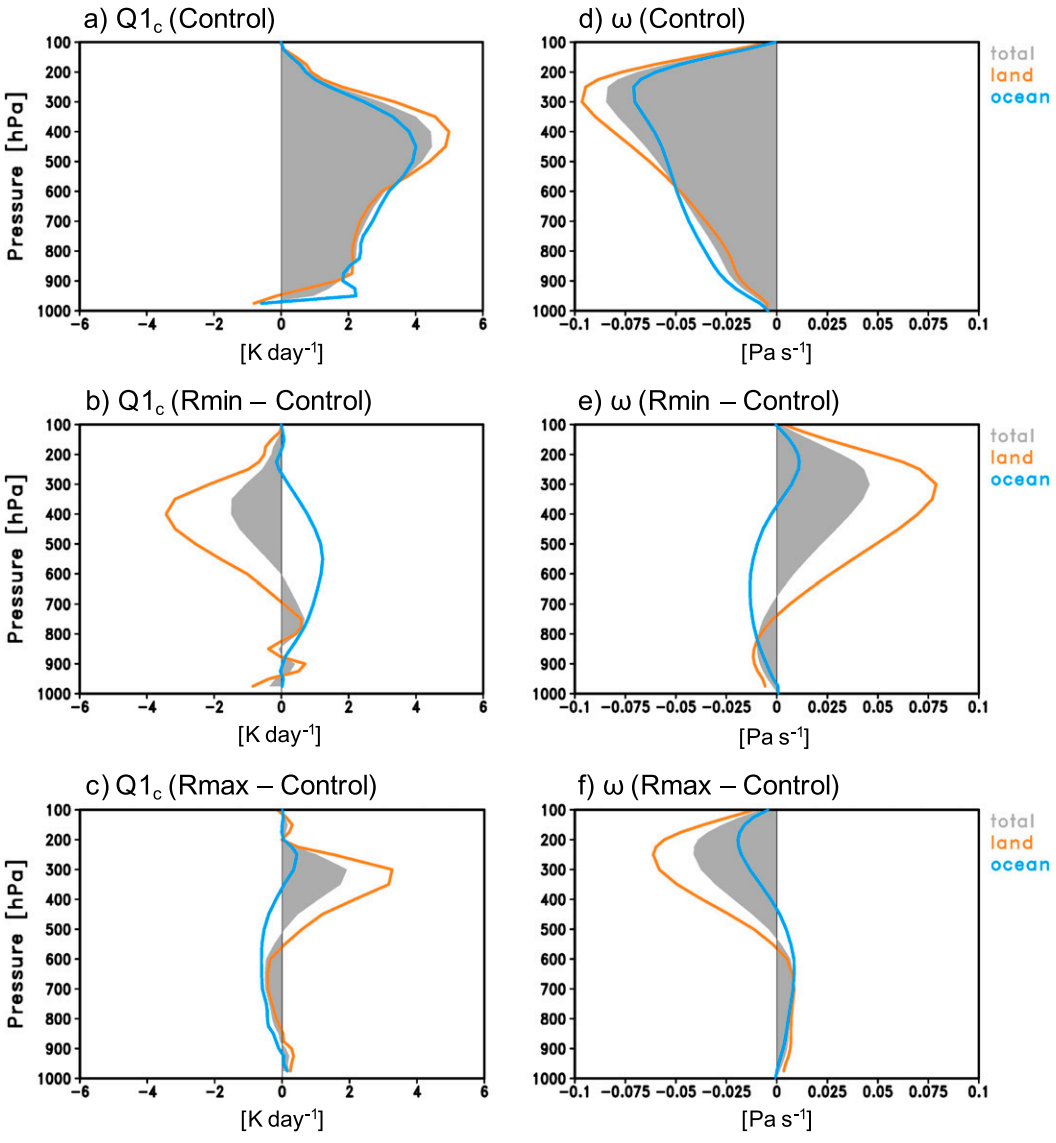

FIG. 2. Area-averaged (5°S–5°N, 100°–120°E) boreal winter (November–April) mean state of (a)–(c) temperature tendency by the model moist processes ($Q1_c$) (K day^{-1}) and (d)–(f) vertical pressure velocity (ω) (Pa s^{-1}): (top) Control, (middle) $R^{\min}$ minus Control, and (bottom) $R_{\max}$ minus Control. Gray, orange, and blue colors indicate total, land, and ocean grid mean, respectively.

changes in the total $Q1_c$ and vertical motion over the MC region are dominated by those in the land grid point, which are partly compensated by the changes in the oceanic grids.

Because the MC resides in the area of the upward branch of the local Walker and Hadley circulations, the changes in the diabatic heating over the MC effectively influence those large-scale circulations (Ramage 1968; Neale and Slingo 2003). Through its influence on local vertical motion, the change in the properties of MC land convection has nonlocal effects on the large-scale circulation and the distribution of the mean precipitation and moisture over the Indo-Pacific warm pool area. Figures 3a–c show the local Walker circulation and its response to the changes in MC land convection. In Control, the upward branch of the local Walker circulation shows its maximum over the MC area (100°–140°E, Fig. 3a). In $R_{\min}$, the upward branch of the Walker circulation weakens over the entire MC area, except in the lower layer, and the vertical motion is enhanced in the Indian Ocean (Fig. 3b). In $R_{\max}$, the upward branch of the Walker circulation strengthens over the western MC area (90°–110°E) with a weakening of the mean vertical motion over the Indian Ocean. The upward branch of the

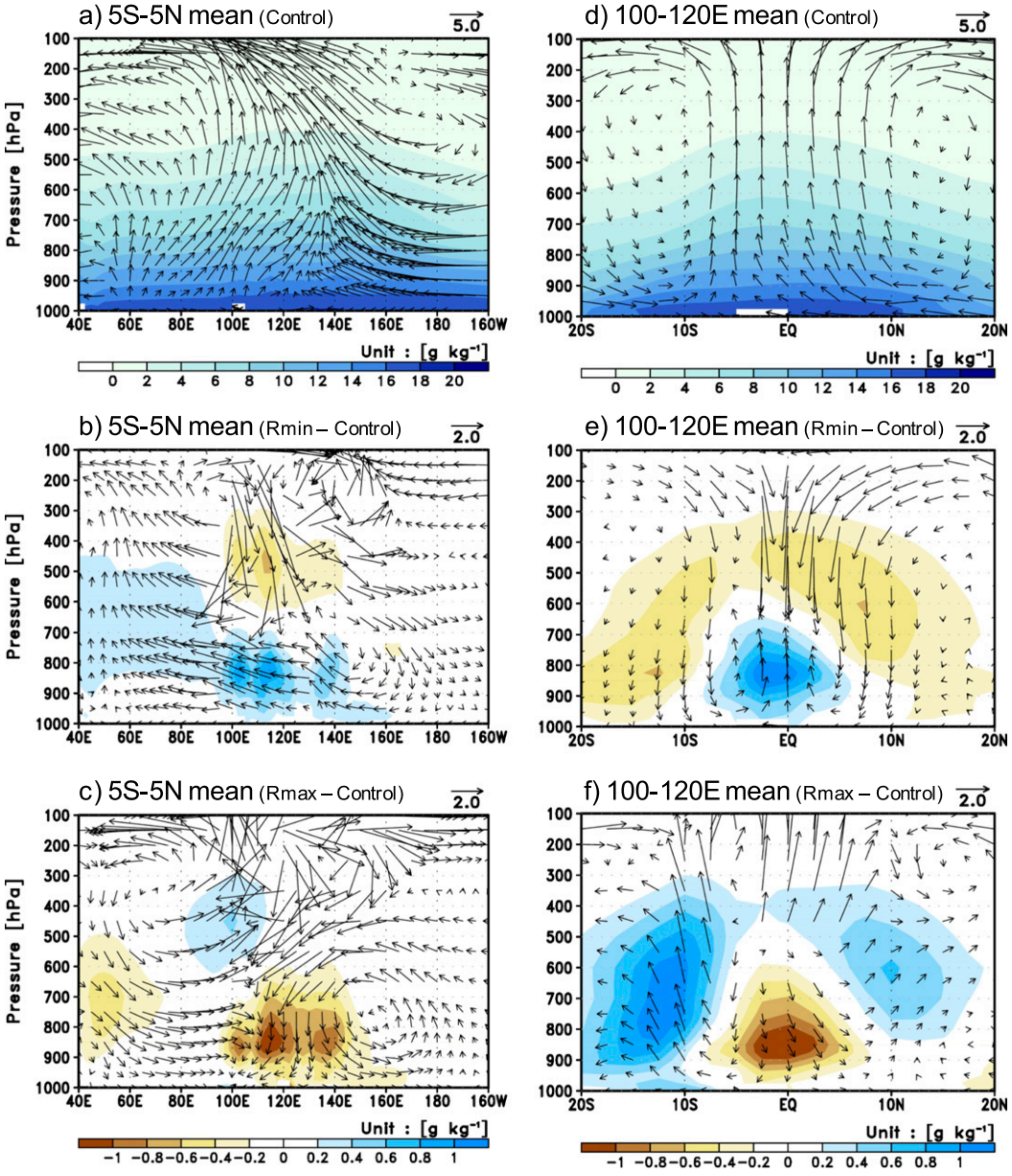

FIG. 3. Boreal winter (November–April) mean state of specific humidity (g kg^{-1}) (shading) and circulation (vector) near the Maritime Continent region: (top) Control, (middle) R_{min} minus Control, and (bottom) R_{max} minus Control, showing (a)–(c) latitudinally (5°S–5°N) averaged values in a longitude–pressure diagram and (d)–(f) longitudinally (100°–120°E) averaged values in a latitude–pressure diagram. The wind vectors are obtained from **u** and $-100 \times \omega$ for the longitude–pressure diagrams and **v** and $-100 \times \omega$ for the latitude–pressure diagrams.

Walker circulation weakens over the eastern MC area throughout the troposphere (Fig. 3c).

Figures 3d–f show the local Hadley circulation in Control and its changes in the R_{min} and R_{max} experiments. In Control, the upward branch of the local Hadley circulation spans from about 10°S to about 10°N, while the mean downward motion prevails poleward of 15°N and 15°S (Fig. 3d). In R_{min}, the mean upward motion in the upward branch of the local Hadley circulation overall weakens, except in the shallow layer below 700-hPa narrowly confined near the equator, in which the mean vertical wind enhances. This circulation change is likely associated with the decreased deep convection and increased shallow convection (Fig. 1b) accompanying less diabatic heating in upper layer and more diabatic heating in lower layer (Fig. 2b) over the MC. The troposphere experiences drying overall, again except below 700-hPa near the equator (Fig. 3e).

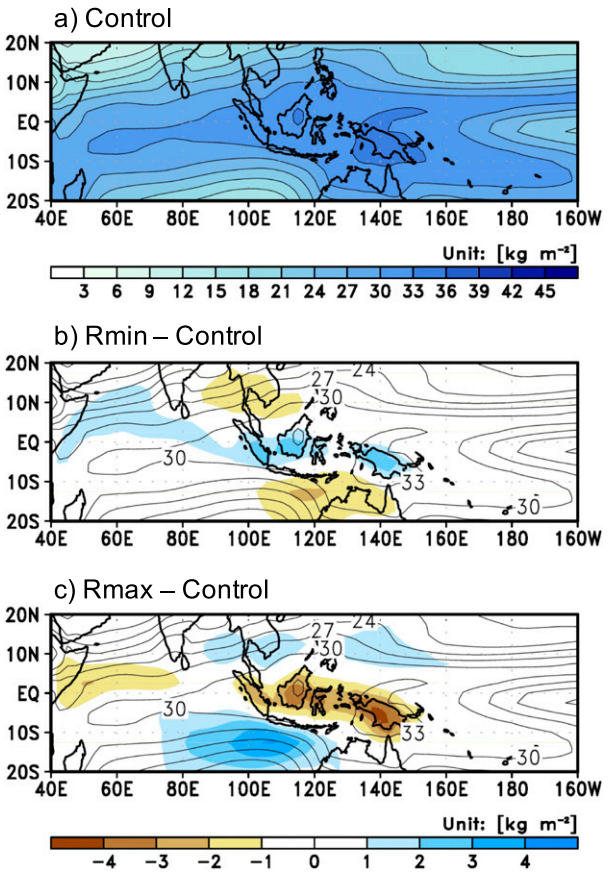

FIG. 4. Horizontal patterns of boreal winter (November–April) mean state of vertically integrated (900–600 hPa) specific humidity ($kg\,m^{-2}$) for (a) Control and the difference from Control for (b) R_{min} and (c) R_{max}, respectively. The contours in (b) and (c) show the mean state pattern for Control.

Figure 4 shows horizontal patterns of the mid- to lower-tropospheric integrated specific humidity. In R_{min}, the mid- to lower-tropospheric mean moisture increases near the equator, especially over the landmasses, and it decreases over the off-equatorial area straddling the MC region (Fig. 4b). In R_{max}, the changes in the zonally averaged circulation and moisture distribution are opposite to those in R_{min} (Figs. 3f and 4c), which is related to the increased deep convection (upper-troposphere heating) and decreased shallow convection (lower-troposphere heating) over the MC (Figs. 1c and 2c).

The above results show that, compared to Control, the zonal and meridional moisture gradients around the MC are more steep in R_{min}, and less steep in R_{max} (Figs. 4b,c). Also, the vertical moisture gradient in the mid- to lower troposphere (500–800-hPa) is increased in R_{min} and decreased in R_{max} (Figs. 3b,e and c,f). In the next subsection, we will examine the effect of the changes in the mean state moisture gradient on MJO propagation.

b. Role of MC land convection on MJO propagation

Figure 5 shows lag–longitude diagrams of the equatorial intraseasonal rain-rate anomalies associated with the MJO obtained by the method described in section 2b in observations and the model simulations. Control captures the observed eastward propagation of MJO rain-rate anomalies although the rain-rate anomalies are slightly weaker than the observed over the MC. Compared to Control, R_{min} exhibits more coherent and pronounced eastward progression of MJO rain-rate anomalies from the western Indian Ocean to the western Pacific. In contrast, R_{max} shows oscillations confined within the Indian Ocean without eastward-propagating features, suggesting that the MJO in R_{max} is unable to propagate through the MC. The stark difference between R_{min} and R_{max} in Fig. 5 suggests that representations of the MJO in the model are significantly affected by the changes in MC land convection. In the following, we focus on the differences between the two simulations with altered MC land convection.

Because the MC consists of many islands and surrounding water with complex land–sea distribution, it is worthwhile to examine spatial patterns of the MJO rain-rate anomalies propagating over the MC to better understand the effect of the MC on MJO propagation. Figure 6 shows the spatial patterns of intraseasonal rain-rate anomalies associated with the MJO at select lag days. At the lag day 0, MJO convection is located over the eastern Indian Ocean in observations and in both experiments. While the peak rain-rate anomalies are similar between the two simulations, the MJO precipitation anomalies cover larger meridional extent to the south in R_{min} than in R_{max}, especially over the south equatorial Indian Ocean (Figs. 6b,c).

Near the equator, narrow, zonally elongated positive rain-rate anomalies appear over the MC area in both simulations, mimicking the observed ''vanguard'' precipitation anomalies (Peatman et al. 2014). In observations, the precipitation anomalies over the MC islands precede the main MJO convection anomalies. This so-called vanguard precipitation signal could appear as a result of the rapid response of diurnal cycle in the MC land area to the frictional and topographic moisture convergence and land convection being enhanced to the east of the main convective envelope due to increase in downward solar radiation at the surface (Peatman et al. 2014). Unlike in observations, however, the model precipitation anomalies near the equator are pronounced over both MC land and ocean area except New Guinea island, suggesting that they might have a different origin. The in-phase structure between low pressure and easterly wind anomalies at lower troposphere over the

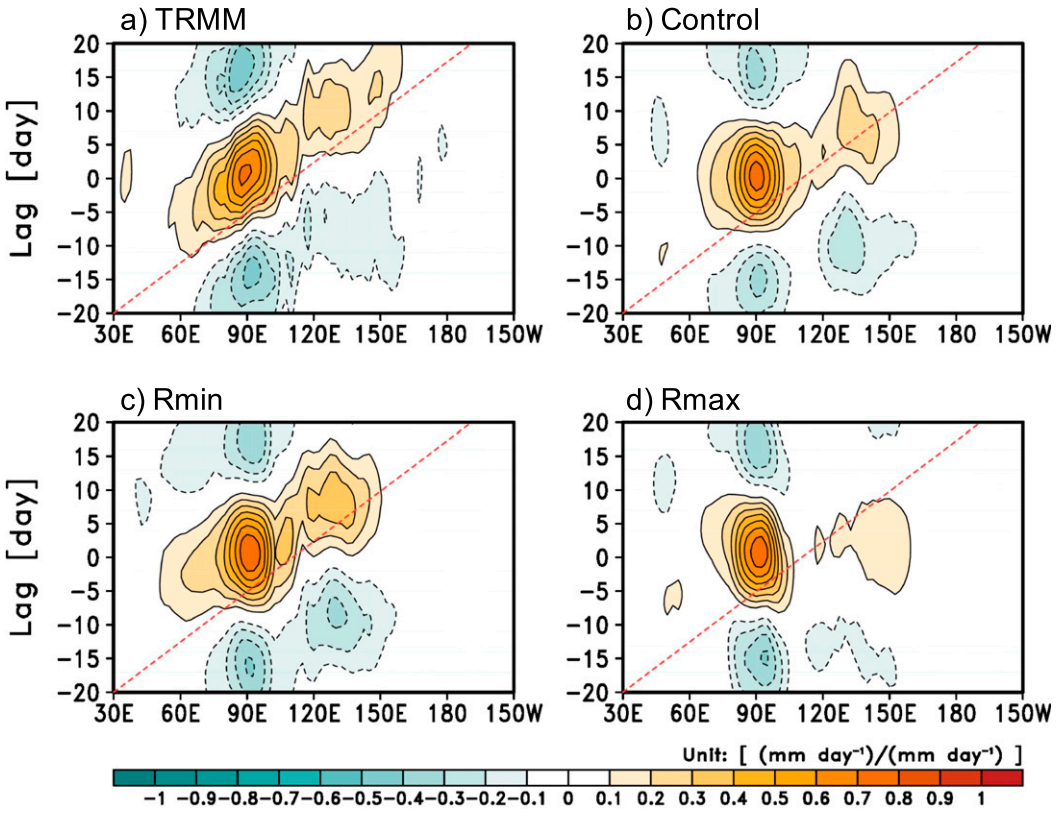

FIG. 5. Lag–longitude diagram of precipitation averaged over 10°S–10°N for (a) TRMM, (b) Control, (c) R_{min}, and (d) R_{max}. The diagram is obtained from the lead–lag regression of 20–100 day filtered precipitation against its area-averaged time series over Indian Ocean (5°S–5°N, 85°–95°E) for boreal winter (November–April). The red line in each panel indicates 5 m s^{-1} eastward propagation speed.

equatorial rainbands (not shown) indicates that the narrow rainbands in the model simulations are likely associated with the convectively coupled Kelvin waves (CCKWs) emanating from the enhanced convection over the IO. There is a notable difference in the distribution of the equatorial rain anomalies between the two simulations. While the rain anomalies cover most of the equatorial MC region (110°–150°E) in R_{min}, they are located over the eastern MC and the west Pacific (130°–170°E) with a weaker signal in the western MC region (100°–120°E) in R_{max}. Over the MC region, the low pressure and easterly wind anomalies associated with the CCKWs are also weaker in R_{max} than that of R_{min} (not shown), suggesting that the coupling of Kelvin wave to moisture and convection is suppressed over most of the MC area in R_{max}.

At the lag day +6, the main MJO envelope is located over the MC region in R_{min} (Fig. 6e). In R_{max}, in contrast, an area of near-zero precipitation anomalies exists over the MC between the decaying MJO main envelope over the eastern Indian Ocean and the decaying CCKW in the west Pacific (Fig. 6f), indicating that the development of rain-rate anomalies in the MC area is suppressed in R_{max}. This result also suggests that the difference in MJO propagation between R_{min} and R_{max} is mainly due to the differences over the MC area (red box in Fig. 6). Between lag day 0 and +6, anomalous convection makes poleward propagation in the eastern Indian Ocean in observations and in the model simulations. Interestingly, the poleward propagation of convection appears to be faster in R_{min} than in R_{max}, mimicking the observed pattern more closely. The faster poleward propagation in R_{min} might be due to the steeper meridional moisture gradient (Fig. 4). Jiang et al. (2018) argued that meridional moisture gradient is an important aspect of the basic state that affects poleward propagation of MJO convection.

At the lag day +12, the main MJO envelope appears in the Timor and Arafura seas with a secondary peak of rain anomalies over the west Pacific in both observations and in R_{min}. In contrast, positive rain-rate anomalies have disappeared over the warm-pool region in R_{max}, except the blob of enhanced precipitation that branched off from the MJO main envelope to the south. It appears that the equatorial region experiences strong drying,

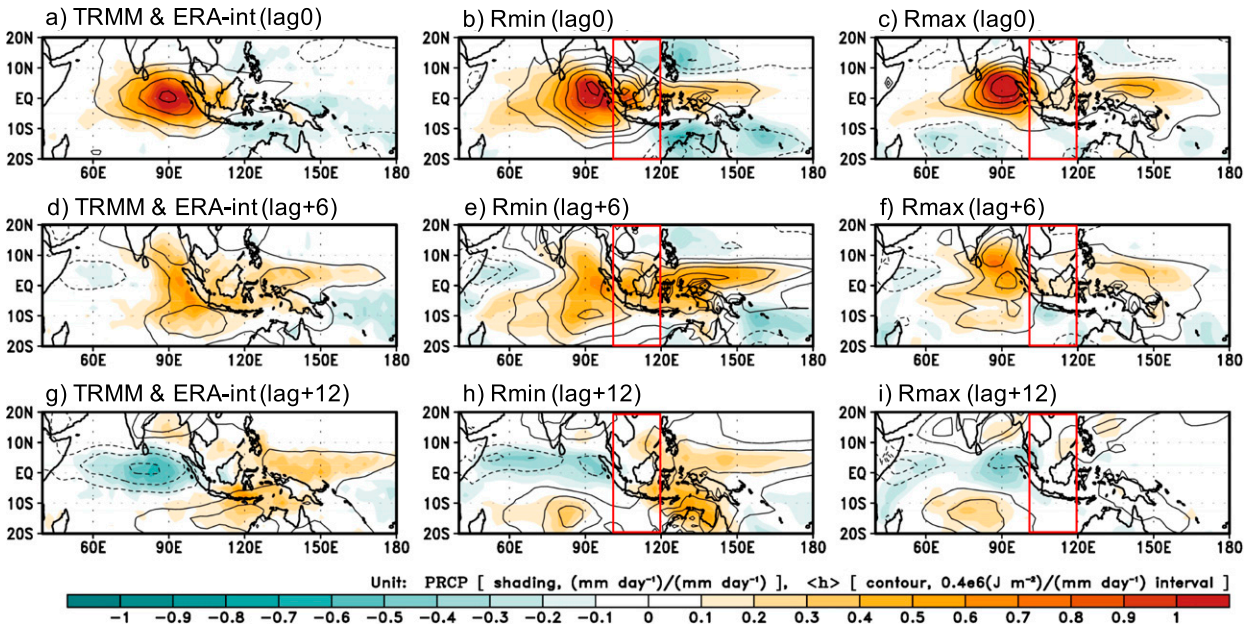

FIG. 6. Lag regressed horizontal patterns of precipitation (shading) and column integrated MSE (contour) anomalies for (left) observations, (middle) R_{min}, and (right) R_{max} at (a)–(c) lag day 0, (d)–(f) lag day +6, and (g)–(i) lag day +12, respectively. The lag regression of each variable is conducted using 20–100 day filtered variable against 20–100 day filtered precipitation averaged over Indian Ocean (5°S–5°N, 85°–95°E) for boreal winter (November–April). Red boxes indicate the western MC area (100°–120°E) where the difference between R_{min} and R_{max} becomes larger before and during the onset of enhanced MJO convection over the Maritime Continent.

while a branch of anomalous convection makes southward propagation in the eastern Indian Ocean, leaving an isolated area of positive rain-rate anomalies in the south Indian Ocean. The blob that is located in the subtropical region (~15°S) seems also to propagate westward, suggesting that Rossby wave dynamics might play a role in the movement of it. The westward-propagating enhanced precipitation blob in the southern Indian Ocean is not present in observations, indicating it is an intrinsic model bias and not much affected by MC land convection.

We now analyze the MSE budget of the simulated MJO with a goal of addressing the following question: why is the development of MJO precipitation anomalies suppressed over the MC in R_{max}? Figure 6 also shows vertically integrated MSE anomalies in addition to the rain-rate anomalies. Hereafter, MSE means column-integrated MSE unless indicated otherwise. The tight coherence of MSE with precipitation shown in Fig. 6 justifies the use of the MSE budget diagnostics to understand the MJO propagation and maintenance mechanisms in this model.

Our MSE budget analysis focuses on the equatorial MC band (5°S–5°N) and the southern MC band (15°–5°S) separately because the timing of MJO propagation is different and the MJO propagation is likely to be influenced by different processes in these two areas. The latter consideration is based on two observed differences between the two regions: (i) most of MC landmasses with steep topography reside in the equatorial MC area, while the southern MC area is mostly covered by water, and (ii) the horizontal mean moisture gradient is much steeper in the southern MC area (Kim et al. 2017).

Figure 7 shows lag–longitude diagrams of intraseasonal MSE (contour) and MSE tendency (shading) anomalies in the near-equatorial and southern MC bands. The MSE and MSE tendency are tightly correlated with each other with a 90° phase shift. In the near-equatorial band (Figs. 7a,b), the difference in the eastward propagation of MSE anomalies between R_{min} and R_{max} becomes larger over the western MC area, which seems to be caused by the difference in MSE tendency from lag −15 to lag 0 days (red box in Figs. 7a,b). In the southern MC band (Figs. 7c,d), while the MSE anomaly in R_{min} shows eastward propagation, no hint of eastward propagation is found in R_{max} and there is a much weaker MSE tendency over the western MC area from lag −10 to lag +5 days (red box in Figs. 7c,d). To identify the major MSE budget terms that are contributing to the difference in MSE tendency over the western MC area, we plotted the MSE budget terms using the method described in section 2b for the equatorial western MC area (5°S–5°N, 100°–120°E) and in the southern western MC area (15°–5°S, 100°–120°E).

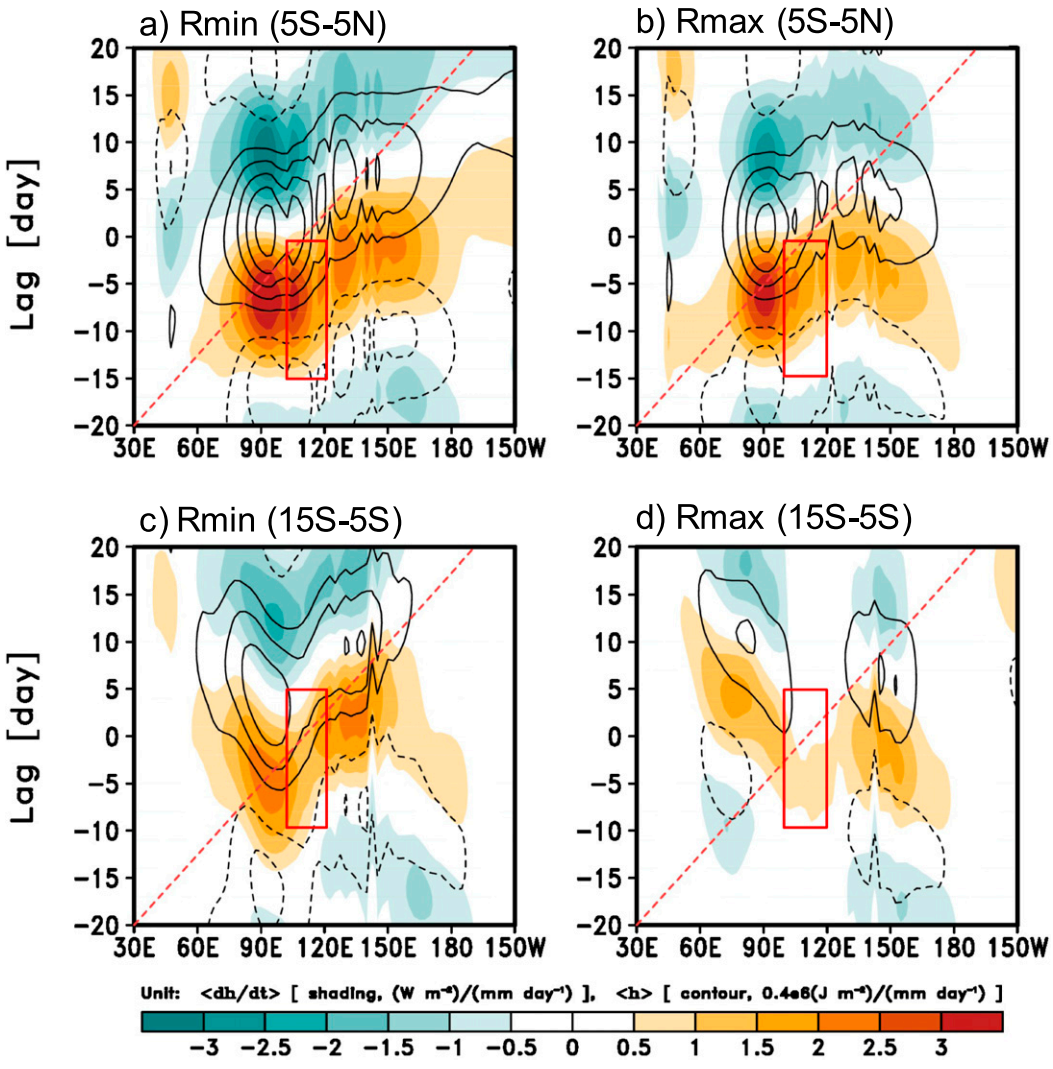

FIG. 7. Lag–longitude diagram of column integrated MSE tendency (shading) and column integrated MSE (contour) averaged over (a),(b) 5°S–5°N and (c),(d) 15°–5°S for (left) R_{min} and (right) R_{max}. The diagram of each variable is obtained from the lead–lag regression of the 20–100-day filtered variable against 20–100-day filtered precipitation averaged over Indian Ocean (5°S–5°N, 85°–95°E) for boreal winter (November–April). The red line in each panel indicates 5 m s^{-1} eastward propagation speed. The red box in each panel indicates the target area and lag days for the MSE budget analysis.

Figure 8 shows that the MSE tendency in R_{min} is about 1.6 and 3 times larger than that in R_{max} in the equatorial western MC (Fig. 8a) and the southern western MC (Fig. 8b), respectively. The larger MSE tendency in R_{min} is mainly due to the larger horizontal and vertical advection terms despite the larger compensation by the longwave radiation and the latent heat flux terms in R_{min}. In the rightmost part in Fig. 8, we show the sum of horizontal advection and surface latent heat flux (HWND) because they are all influenced by low-level MJO horizontal wind anomalies and the sum of the vertical advection and column-integrated longwave heating (CONV) as they are strongly tied to local convective activity. Note that, unlike in Chikira (2014), in which the sum of vertical advection, cloud microphysical processes, radiative heating, and vertical diffusion is considered as the ''column process,'' we consider in CONV only the terms that are closely related to the local convective activity.

In the equatorial western MC area, the difference in CONV dominates, indicating that the processes that are linked to local convective activity are responsible for the MSE tendency difference between R_{min} and R_{max}. In particular, vertical advection of MSE is much stronger in R_{min} than in R_{max}. The opposite is the case in the southern western MC area, with a much greater difference

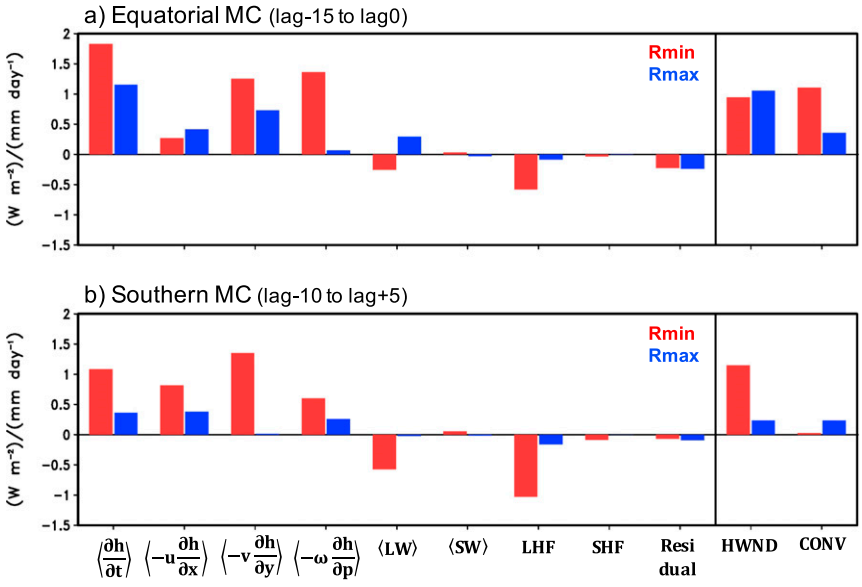

FIG. 8. Column integrated MSE budget terms lead–lag regressed onto 20–100-day filtered precipitation averaged over Indian Ocean (5°S–5°N, 85°–95°E) for boreal winter (November–April) and averaged over (a) the equatorial MC region (5°S–5°N, 100°–120°E) during lag −15 to lag 0 days and (b) the southern MC region (15°–5°S, 100°–120°E) during lag −10 to lag +5 days for R_{min} (red) and R_{max} (blue). HWND and CONV on the x axis indicate the sum of terms related to horizontal wind intensity (horizontal advection and surface latent heat flux) and convective activity (vertical advection and column-integrated longwave heating), respectively.

appearing in HWND. In this region, the difference is dominated by that in meridional MSE advection.

To better understand the source of the difference in vertical and meridional MSE advection terms, each advection term is decomposed using the method described in section 2b (Fig. 9). In both vertical and meridional advection terms, the advection of low-frequency mean MSE by MJO perturbation wind is the dominant term that is responsible for the larger MSE advection in R_{min}. It suggests that steeper low-frequency mean MSE

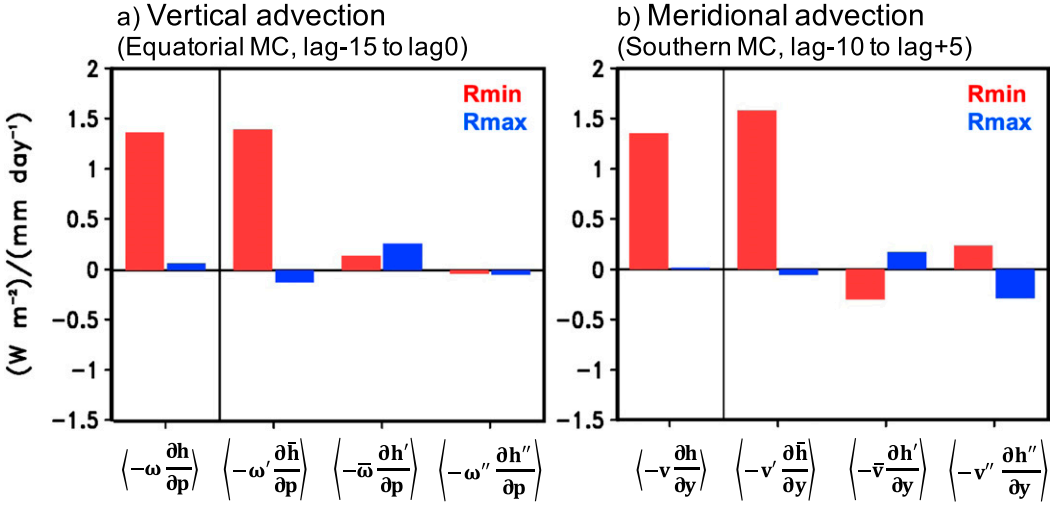

FIG. 9. Column integrated MSE (a) vertical advection and (b) meridional advection terms with time decomposition lead–lag regressed onto 20–100-day filtered precipitation averaged over the Indian Ocean (5°S–5°N, 85°–95°E) for boreal winter (November–April) for R_{min} (red) and R_{max} (blue). In (a) and (b), the terms are averaged over the equatorial MC region (5°S–5°N, 100°–120°E) during lag −15 to lag 0 days and over the southern MC region (15°–5°S, 100°–120°E) during lag −10 to lag +5 days, respectively.

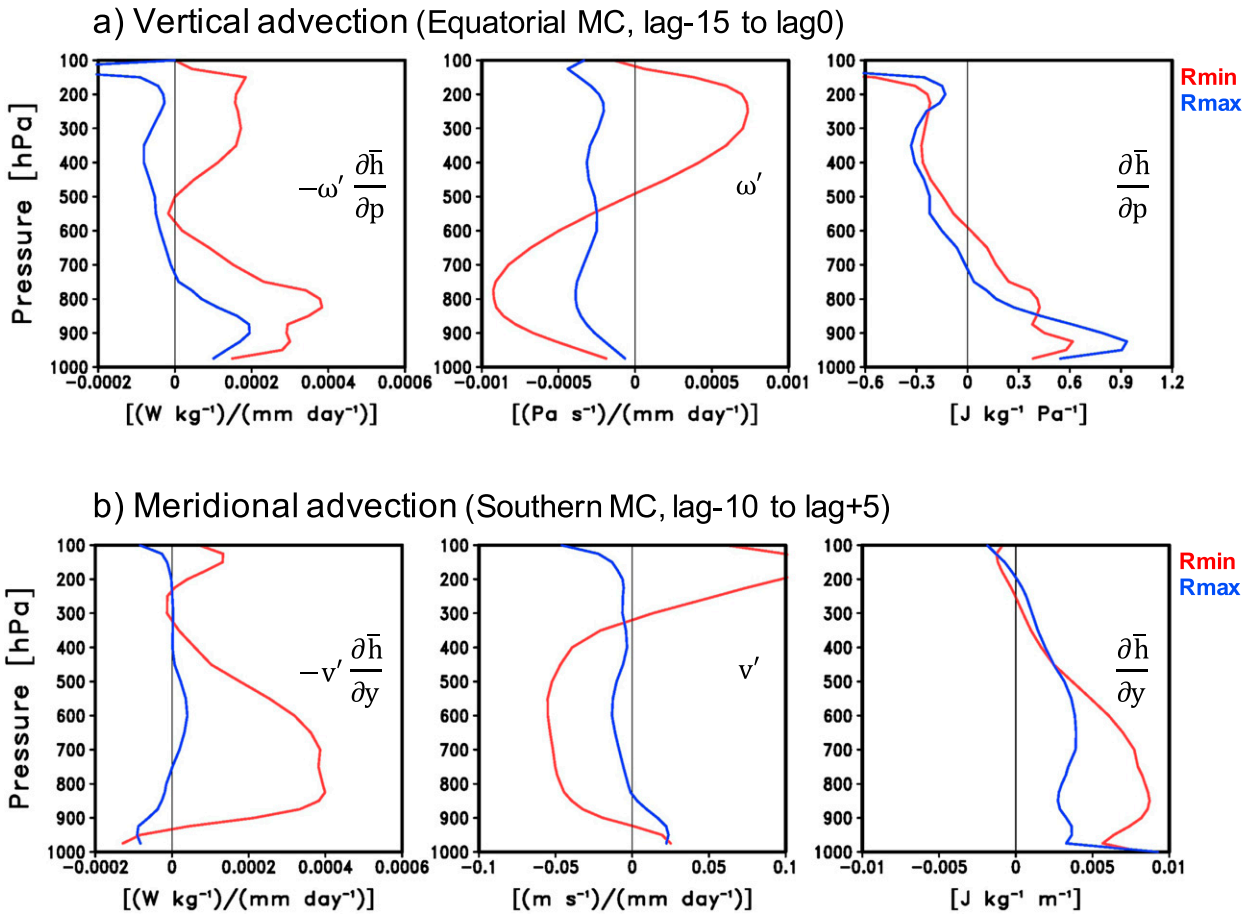

FIG. 10. Vertical profiles of (left) mean MSE advection by MJO perturbation wind and (middle) MJO perturbation wind lead–lag regressed onto 20–100-day filtered precipitation averaged over Indian Ocean (5°S–5°N, 85°–95°E) for boreal winter (November–April), and (right) boreal winter mean MSE gradient for (a) vertical advection and (b) meridional advection. In (a) and (b), the terms are averaged over the equatorial MC region (5°S–5°N, 100°–120°E) and over the southern MC region (15°–5°S, 100°–120°E), respectively. For the lead–lag regressed terms in (left) and (middle), lag −15 to lag 0 and lag −10 to lag +5 are averaged for (a) and (b), respectively. Red and blue curves indicate R_{min} and R_{max}, respectively.

gradient and stronger MJO perturbation wind are key factors that enhance the MSE advection, and hence the MSE tendency over the MC.

To further examine the role of the mean MSE gradient and MJO perturbation wind in the advection terms, we show vertical profiles of the seasonal mean MSE gradient and the MJO wind anomalies together with the mean MSE advection by MJO perturbation wind term in Fig. 10. R_{min} shows stronger positive vertical advection anomalies in the mid- to lower troposphere than R_{max} over the equatorial western MC (Fig. 10a), which can be attributed to both stronger upward MJO perturbation wind and steeper mean MSE vertical gradient, except in the boundary layer below 850 hPa. Also, the vertical advection in mid- to upper-tropospheric levels is larger in R_{min} due to the stronger downward MJO perturbation wind than that of R_{max}. The stronger downward MJO perturbation wind shown here is related to the suppressed convection associated with MJO dipole structure before the MJO convection arrives on the western MC. In the meridional advection over the southern western MC (Fig. 10b), the advection in mid- to lower-tropospheric levels is larger in R_{min}. The larger meridional advection in R_{min} is due to the stronger northerly MJO perturbation wind and the steeper meridional gradient of the mean MSE. Our MSE budget analysis pinpoints both stronger MJO wind anomalies and the steeper mean MSE gradient as the factors that are responsible for the difference between R_{min} and R_{max} in their representation of the MJO's propagation.

It is worthwhile to note that the magnitude of MJO wind anomalies is tightly related to the magnitude of the MJO convection and the associated suppressed convection (Kim et al. 2014; Chen and Wang 2018) because the MJO perturbation wind field is formed as a wave response to the MJO convective heating in the tropics

(Gill 1980; Adames and Kim 2016; Wang et al. 2018). Therefore, the stronger MJO wind anomalies in R_{min} cannot be the cause of the change in MJO intensity at the first stage of MJO development although it can give a positive feedback to MJO convection to grow further. On contrary, attributing the difference in MJO intensity to the mean state differences is free from the causality issue because the mean state can be considered as external to the MJO variability. The mean state moisture of 101-day moving average data in which the moisture variation associated with MJO is removed is almost same with the mean state moisture of raw data (not shown). Here we are assuming there is no nonlinear rectification of MJO activity and its impacts on the MJO. Therefore, it is reasonable to conclude that the difference in the mean MSE gradient between R_{min} and R_{max} is likely the factor that made the difference between the two simulations. With a steeper mean MSE gradient, the MJO in R_{min} can be maintained longer, propagate and grow further, and MJO wind anomalies would be stronger as a result and give a positive feedback to growth of the MJO convection. Our result suggests that the vertical and meridional moisture gradient around the MC is the key aspect of the mean state that affects MJO propagation over the MC, which is consistent with previous studies that emphasized the importance of mean moisture gradient on MJO propagation (e.g., Gonzalez and Jiang 2017; Kim et al. 2017; Kim 2017).

4. Summary and discussion

The MJO behaves differently in the MC region than over the open water: it tends to detour the MC islands and its eastward propagation is often disrupted in the MC region (see a recent review by Kim et al. 2020). Despite the robustness in observations, our understanding of these peculiar behaviors of the MJO in the MC region is still limited and models poorly represent them. In particular, the way the strong diurnal cycle of convection in and around the MC islands interacts with MJO circulation and convection has remained elusive. Motivated by many recent studies that emphasized the role of the mean state moisture distribution in the propagation of the MJO, we performed a modeling study with a specific goal of examining the effects of MC land convection on the mean state, especially that of moisture distribution around the MC region, and on the MJO's eastward propagation.

With a GCM that simulates a realistic MJO, we performed three 20-yr AMIP-type simulations. In the control simulation, the default convection scheme (UNICON) is used without any modifications. One of the key parameters in UNICON is the updraft plume radius, which is calculated interactively within the scheme and affects the depth of simulated convection via its effects on the lateral entrainment rate and other plume properties. To force convection over the MC landmasses to be deeper and shallower, the updraft plume radius is set to its minimum (R_{min}) and maximum (R_{max}) value only in the MC land grids, respectively.

The results show that convective cloud top height and rain rate over the MC land area decrease (increase) in R_{min} (R_{max}), with compensating changes in rain rate over the adjacent water. The vertical structures of diabatic heating and vertical motion show that they become more bottom heavy (top heavy) in R_{min} (R_{max}) compared to the control simulation, which is the change that is dominated by those over the MC island. The changes in the vertical structure of diabatic heating and vertical motion are consistent with the changes in cloud type—mostly deep in R_{max} and mostly shallow in R_{min}.

The changes in cloud type and the vertical structure of diabatic heating are associated with the local Walker and Hadley circulations and the three-dimensional distribution of the mean moisture. In R_{min}, upward motion strengthens below 700 hPa and while it weakens above 700 hPa in the upward branch of the local Hadley circulation over the equatorial MC region. The enhanced and weakened vertical motion in the lower and upper troposphere is accompanied by an increased and decreased moisture content, respectively. With this moisture content change, the mean vertical moisture gradient steepens in R_{min}. Meanwhile, the sinking motion in the downward branch of the local Hadley circulation strengthens in R_{min}, drying the off-equatorial MC area. As a result, the meridional and vertical gradient of the mean moisture in the MC region increases in R_{min}. The changes in the mean circulation and moisture in R_{max} mirror those in R_{min}, except with an opposite sign.

Compared to the control simulation, R_{min} simulates more pronounced MJO propagation over the MC, whereas R_{max} shows a standing wave-like oscillation over the Indian Ocean. To identify the processes that are responsible for the difference in MJO propagation between the two experiments, we analyzed the MSE budget of the MJO. The MSE budget analysis focused on the western MC area, in which the two simulations exhibit a marked difference. The MSE budget analysis was performed for the equatorial and southern western MC areas, separately, because the two regions feature different land–sea contrast and the mean moisture gradient.

The MSE budget analysis revealed that the vertical and meridional advection of the mean MSE by MJO perturbation winds are the dominant processes that are responsible for the difference between the two experiments in MJO propagation, highlighting the role of the mean

MSE (moisture) gradient. Moreover, there is an interesting regional difference. In the equatorial MC region, it is vertical MSE advection that shows the largest difference between R_{min} and R_{max}. In the southern MC region, however, the meridional MSE advection most of the difference in MJO MSE budget between R_{min} and SLMC.

In many contemporary GCMs, the MJO rarely propagates through the MC (Kim et al. 2009; Hung et al. 2013; Jiang et al. 2015; Ahn et al. 2017). Gonzalez and Jiang (2017) suggested that this common model bias might be linked to the bias in the mean moisture distribution around the MC. They showed that the correlation between MJO propagation skills and mean moisture pattern skills over the MC is about 0.8 across 23 GCM simulations. They also presented that the main difference in the mean moisture distribution between the good and poor MJO models is in the equatorial MC area, where the mid- to lower troposphere is systematically wetter in the good MJO models. We also found that the MJO is much better represented in the simulation in which the equatorial MC area has more moisture in the lower troposphere (R_{min} versus R_{max}). Our results together with those in Gonzalez and Jiang (2017) strongly suggest that the exaggerated MC barrier effect on MJO propagation in some models may be caused by biases in the meridional and vertical mean moisture gradients around the MC region. Our result also suggests that the bias in the mean state moisture gradient in some models may be influenced by that of the MC land convection. Baranowski et al. (2019) showed that many contemporary GCMs exhibit biases in the diurnal cycle of precipitation over the MC islands. In this sense, it would be worthwhile to examine the simulation skill of MC land convection for the models that simulate dry bias in the mid- to lower-tropospheric MC area. For the models with the dry bias, our results suggest that improving the representation of MC land convective intensity and convective top height (convective heating level) could help improve the mean state moisture.

Previous work has suggested that the convection over the MC region, especially those associated with diurnal cycle, plays a critical role in the mean state (e.g., Neale and Slingo 2003). Our modeling study is the first one in which the effect of MC land convection is isolated from those of land–sea contrast and topography. While our work shed some new lights on the role of the MC land convection in shaping the mean moisture pattern, more work is needed to better understand the factor that controls the mean state, especially moisture distribution, in observations and models.

Acknowledgments. MSA and DK were supported by the NOAA's Climate Program Office's Climate Variability and Predictability program through Grant NA18OAR4310300, the U.S. Department of Energy's Regional and Global Model Analysis program under Grant DE-SC0016223, the National Aeronautics and Space Administration's Modeling, Analysis, and Prediction program under Grant 80NSSC17K0227. YGH was supported by the Basic Science Research Program through the National Research Foundation of Korea (NRF) funded by the Ministry of Education (NRF-2016R1A6A1A03012647). DK and YGH were also supported by Korean Meteorological Administration Research and Development Program under Grant KMI2018-03110. SP was supported by Seoul National University. We thank Hyemi Kim and Chidong Zhang for their constructive comments and Jihoon Shin for his help configure the model experiments. We would like to acknowledge high-performance computing support from Cheyenne (https://doi.org/10.5065/D6RX99HX) provided by NCAR's Computational and Information Systems Laboratory, sponsored by the National Science Foundation. The Tropical Rainfall Measuring Mission (TRMM), a joint mission of the National Aeronautics and Space Administration (NASA) and the Japan Aerospace Exploration Agency, provided the precipitation data (https://pmm.nasa.gov/data-access/downloads/trmm). The European Centre for Medium-Range Weather Forecasts (ECMWF) provided the ERA-Interim reanalysis data (https://apps.ecmwf.int/datasets/).

REFERENCES

Adames, Á. F., and D. Kim, 2016: The MJO as a dispersive, convectively coupled moisture wave: Theory and observations. *J. Atmos. Sci.*, **73**, 913–941, https://doi.org/10.1175/JAS-D-15-0170.1.

——, J. M. Wallace, and J. M. Monteiro, 2016: Seasonality of the structure and propagation characteristics of the MJO. *J. Atmos. Sci.*, **73**, 3511–3526, https://doi.org/10.1175/JAS-D-15-0232.1.

——, D. Kim, A. H. Sobel, A. Del Genio, and J. Wu, 2017: Characterization of moist processes associated with changes in the propagation of the MJO with increasing CO_2. *J. Adv. Model. Earth Syst.*, **9**, 2946–2967, https://doi.org/10.1002/2017MS001040.

Ahn, M.-S., D. Kim, K. R. Sperber, I.-S. Kang, E. Maloney, D. Waliser, and H. Hendon, 2017: MJO simulation in CMIP5 climate models: MJO skill metrics and process-oriented diagnosis. *Climate Dyn.*, **49**, 4023–4045, https://doi.org/10.1007/s00382-017-3558-4.

——, ——, S. Park, and Y.-G. Ham, 2019: Do we need to parameterize mesoscale convective organization to mitigate the MJO-mean state trade-off? *Geophys. Res. Lett.*, **46**, 2293–2301, https://doi.org/10.1029/2018GL080314.

Andersen, J. A., and Z. Kuang, 2012: Moist static energy budget of MJO-like disturbances in the atmosphere of a zonally symmetric aquaplanet. *J. Climate*, **25**, 2782–2804, https://doi.org/10.1175/JCLI-D-11-00168.1.

Arnold, N. P., Z. Kuang, and E. Tziperman, 2013: Enhanced MJO-like variability at high SST. *J. Climate*, **26**, 988–1001, https://doi.org/10.1175/JCLI-D-12-00272.1.

——, M. Branson, Z. Kuang, D. A. Randall, and E. Tziperman, 2015: MJO intensification with warming in the superparameterized CESM. *J. Climate*, **28**, 2706–2724, https://doi.org/10.1175/JCLI-D-14-00494.1.

Baranowski, D. B., D. E. Waliser, X. Jiang, J. A. Ridout, and M. K. Flatau, 2019: Contemporary GCM fidelity in representing the diurnal cycle of precipitation over the Maritime Continent. *J. Geophys. Res. Atmos.*, **124**, 747–769, https://doi.org/10.1029/2018JD029474.

Chen, G., and B. Wang, 2018: Effects of enhanced front Walker cell on the eastward propagation of the MJO. *J. Climate*, **31**, 7719–7738, https://doi.org/10.1175/JCLI-D-17-0383.1.

Chikira, M., 2014: Eastward-propagating intraseasonal oscillation represented by Chikira–Sugiyama cumulus parameterization. Part II: Understanding moisture variation under weak temperature gradient balance. *J. Atmos. Sci.*, **71**, 615–639, https://doi.org/10.1175/JAS-D-13-038.1.

Dee, D. P., and Coauthors, 2011: The ERA-Interim reanalysis: Configuration and performance of the data assimilation system. *Quart. J. Roy. Meteor. Soc.*, **137**, 553–597, https://doi.org/10.1002/qj.828.

DeMott, C. A., B. O. Wolding, E. D. Maloney, and D. A. Randall, 2018: Atmospheric mechanisms for MJO decay over the Maritime Continent. *J. Geophys. Res. Atmos.*, **123**, 5188–5204, https://doi.org/10.1029/2017JD026979.

Eyring, V., S. Bony, G. A. Meehl, C. A. Senior, B. Stevens, R. J. Stouffer, and K. E. Taylor, 2016: Overview of the Coupled Model Intercomparison Project Phase 6 (CMIP6) experimental design and organization. *Geosci. Model Dev.*, **9**, 1937–1958, https://doi.org/10.5194/gmd-9-1937-2016.

Feng, J., T. Li, and W. Zhu, 2015: Propagating and nonpropagating MJO events over Maritime Continent. *J. Climate*, **28**, 8430–8449, https://doi.org/10.1175/JCLI-D-15-0085.1.

Fuchs, Ž., and D. J. Raymond, 2017: A simple model of intraseasonal oscillations. *J. Adv. Model. Earth Syst.*, **9**, 1195–1211, https://doi.org/10.1002/2017MS000963.

Gill, A. E., 1980: Some simple solutions for heat-induced tropical circulation. *Quart. J. Roy. Meteor. Soc.*, **106**, 447–462, https://doi.org/10.1002/qj.49710644905.

Gonzalez, A. O., and X. Jiang, 2017: Winter mean lower tropospheric moisture over the Maritime Continent as a climate model diagnostic metric for the propagation of the Madden-Julian oscillation. *Geophys. Res. Lett.*, **44**, 2588–2596, https://doi.org/10.1002/2016GL072430.

Hagos, S. M., C. Zhang, Z. Feng, C. D. Burleyson, C. De Mott, B. Kerns, J. J. Benedict, and M. N. Martini, 2016: The impact of the diurnal cycle on the propagation of Madden-Julian Oscillation convection across the Maritime Continent. *J. Adv. Model. Earth Syst.*, **8**, 1552–1564, https://doi.org/10.1002/2016MS000725.

Hsu, H. H., and M. Y. Lee, 2005: Topographic effects on the eastward propagation and initiation of the Madden–Julian oscillation. *J. Climate*, **18**, 795–809, https://doi.org/10.1175/JCLI-3292.1.

Huffman, G. J., and Coauthors, 2007: The TRMM Multisatellite Precipitation Analysis (TMPA): Quasi-global, multiyear, combined-sensor precipitation estimates at fine scales. *J. Hydrometeor.*, **8**, 38–55, https://doi.org/10.1175/JHM560.1.

Hung, M. P., J. L. Lin, W. Wang, D. Kim, T. Shinoda, and S. J. Weaver, 2013: MJO and convectively coupled equatorial waves simulated by CMIP5 climate models. *J. Climate*, **26**, 6185–6214, https://doi.org/10.1175/JCLI-D-12-00541.1.

Jiang, X., 2017: Key processes for the eastward propagation of the Madden-Julian Oscillation based on multimodel simulations. *J. Geophys. Res. Atmos.*, **122**, 755–770, https://doi.org/10.1002/2016JD025955.

——, and Coauthors, 2015: Vertical structure and physical processes of the Madden-Julian oscillation: Exploring key model physics in climate simulations. *J. Geophys. Res. Atmos.*, **120**, 4718–4748, https://doi.org/10.1002/2014JD022375.

——, Á. F. Adames, M. Zhao, D. Waliser, and E. Maloney, 2018: A unified moisture mode framework for seasonality of the Madden–Julian oscillation. *J. Climate*, **31**, 4215–4224, https://doi.org/10.1175/JCLI-D-17-0671.1.

Kim, D., and Coauthors, 2009: Application of MJO simulation diagnostics to climate models. *J. Climate*, **22**, 6413–6436, https://doi.org/10.1175/2009JCLI3063.1.

——, J. S. Kug, and A. H. Sobel, 2014: Propagating versus nonpropagating Madden–Julian oscillation events. *J. Climate*, **27**, 111–125, https://doi.org/10.1175/JCLI-D-13-00084.1.

——, H. Kim, and M. I. Lee, 2017: Why does the MJO detour the Maritime Continent during austral summer? *Geophys. Res. Lett.*, **44**, 2579–2587, https://doi.org/10.1002/2017GL072643.

——, E. D. Maloney, and C. Zhang, 2020: Review: MJO propagation over the Maritime Continent. *The Multiscale Global Monsoon System*, C. P. Chang et al., Eds., Vol. 11, World Scientific Series on Asia-Pacific Weather and Climate, World Scientific, in press.

Kim, H. M., 2017: The impact of the mean moisture bias on the key physics of MJO propagation in the ECMWF reforecast. *J. Geophys. Res. Atmos.*, **122**, 7772–7784, https://doi.org/10.1002/2017JD027005.

——, D. Kim, F. Vitart, V. E. Toma, J. S. Kug, and P. J. Webster, 2016: MJO propagation across the Maritime Continent in the ECMWF ensemble prediction system. *J. Climate*, **29**, 3973–3988, https://doi.org/10.1175/JCLI-D-15-0862.1.

——, F. Vitart, and D. E. Waliser, 2018: Prediction of the Madden–Julian oscillation: A review. *J. Climate*, **31**, 9425–9443, https://doi.org/10.1175/JCLI-D-18-0210.1.

Kiranmayi, L., and E. D. Maloney, 2011: Intraseasonal moist static energy budget in reanalysis data. *J. Geophys. Res.*, **116**, D21117, https://doi.org/10.1029/2011JD016031.

Lau, W. K.-M., and D. E. Waliser, 2012: *Intraseasonal Variability in the Atmosphere-Ocean Climate System*. Springer, 614 pp., https://doi.org/10.1007/978-3-642-13914-7.

Ling, J., C. Zhang, S. Wang, and C. Li, 2017: A new interpretation of the ability of global models to simulate the MJO. *Geophys. Res. Lett.*, **44**, 5798–5806, https://doi.org/10.1002/2017GL073891.

——, ——, R. Joyce, P. Xie, and G. Chen, 2019: Possible role of the diurnal cycle in land convection in the barrier effect on the MJO by the Maritime Continent. *Geophys. Res. Lett.*, **46**, 3001–3011, https://doi.org/10.1029/2019GL081962.

Madden, R. A., and P. R. Julian, 1971: Detection of a 40–50 day oscillation in the zonal wind in the tropical Pacific. *J. Atmos. Sci.*, **28**, 702–708, https://doi.org/10.1175/1520-0469(1971)028<0702:DOADOI>2.0.CO;2.

——, and ——, 1972: Description of global-scale circulation cells in the tropics with a 40–50 day period. *J. Atmos. Sci.*, **29**, 1109–1123, https://doi.org/10.1175/1520-0469(1972)029<1109:DOGSCC>2.0.CO;2.

Maloney, E. D., 2009: The moist static energy budget of a composite tropical intraseasonal oscillation in a climate model. *J. Climate*, **22**, 711–729, https://doi.org/10.1175/2008JCLI2542.1.

Neale, R., and J. Slingo, 2003: The Maritime Continent and its role in the global climate: A GCM study. *J. Climate*, **16**, 834–848, https://doi.org/10.1175/1520-0442(2003)016<0834:TMCAIR>2.0.CO;2.

——, and Coauthors, 2012: Description of the NCAR Community Atmosphere Model (CAM 5.0). NCAR Tech. Note NCAR/TN-486+STR, 289 pp.

Park, S., 2014a: A unified convection scheme (UNICON). Part I: Formulation. *J. Atmos. Sci.*, **71**, 3902–3930, https://doi.org/10.1175/JAS-D-13-0233.1.

——, 2014b: A unified convection scheme (UNICON). Part II: Simulation. *J. Atmos. Sci.*, **71**, 3931–3973, https://doi.org/10.1175/JAS-D-13-0234.1.

——, and C. S. Bretherton, 2009: The University of Washington shallow convection and moist turbulence schemes and their impact on climate simulations with the Community Atmosphere Model. *J. Climate*, **22**, 3449–3469, https://doi.org/10.1175/2008JCLI2557.1.

——, ——, and P. J. Rasch, 2014: Integrating cloud processes in the Community Atmosphere Model, version 5. *J. Climate*, **27**, 6821–6856, https://doi.org/10.1175/JCLI-D-14-00087.1.

——, E.-H. Baek, B.-M. Kim, and S.-J. Kim, 2017: Impact of detrained cumulus on climate simulated by the Community Atmosphere Model Version 5 with a unified convection scheme. *J. Adv. Model. Earth Syst.*, **9**, 1399–1411, https://doi.org/10.1002/2016MS000877.

——, J. Shin, S. Kim, E. Oh, and Y. Kim, 2019: Global climate simulated by the Seoul National University Atmosphere Model version 0 with a Unified Convection Scheme (SAM0-UNICON). *J. Climate*, **32**, 2917–2949, https://doi.org/10.1175/JCLI-D-18-0796.1.

Peatman, S. C., A. J. Matthews, and D. P. Stevens, 2014: Propagation of the Madden–Julian Oscillation through the Maritime Continent and scale interaction with the diurnal cycle of precipitation. *Quart. J. Roy. Meteor. Soc.*, **140**, 814–825, https://doi.org/10.1002/qj.2161.

Ramage, C. S., 1968: Role of a tropical "Maritime Continent" in the atmospheric circulation. *Mon. Wea. Rev.*, **96**, 365–370, https://doi.org/10.1175/1520-0493(1968)096<0365:ROATMC>2.0.CO;2.

Raymond, D. J., and Ž. Fuchs, 2009: Moisture modes and the Madden–Julian oscillation. *J. Climate*, **22**, 3031–3046, https://doi.org/10.1175/2008JCLI2739.1.

Seo, K.-H., W. Wang, J. Gottschalck, Q. Zhang, J.-K. E. Schemm, W. R. Higgins, and A. Kumar, 2009: Evaluation of MJO forecast skill from several statistical and dynamical forecast models. *J. Climate*, **22**, 2372–2388, https://doi.org/10.1175/2008JCLI2421.1.

Sobel, A., E. Maloney, 2012: An idealized semi-empirical framework for modeling the Madden–Julian oscillation. *J. Atmos. Sci.*, **69**, 1691–1705, https://doi.org/10.1175/JAS-D-11-0118.1.

——, and ——, 2013: Moisture modes and the eastward propagation of the MJO. *J Atmos. Sci.*, **70**, 187–192, https://doi.org/10.1175/JAS-D-12-0189.1.

——, ——, G. Bellon, and D. M. Frierson, 2010: Surface fluxes and tropical intraseasonal variability: A reassessment. *J. Adv. Model. Earth Syst.*, 2 (2), https://doi.org/10.3894/JAMES.2010.2.2.

Stachnik, J. P., D. E. Waliser, and A. J. Majda, 2015: Precursor environmental conditions associated with the termination of Madden–Julian oscillation events. *J. Atmos. Sci.*, **72**, 1908–1931, https://doi.org/10.1175/JAS-D-14-0254.1.

Tseng, W., H. Hsu, N. Keenlyside, C. J. Chang, B. Tsuang, C. Tu, and L. Jiang, 2017: Effects of surface orography and land–sea contrast on the Madden–Julian oscillation in the Maritime Continent: A numerical study using ECHAM5-SIT. *J. Climate*, **30**, 9725–9741, https://doi.org/10.1175/JCLI-D-17-0051.1.

Vitart, F., S. Woolnough, M. A. Balmaseda, and A. M. Tompkins, 2007: Monthly forecast of the Madden–Julian oscillation using a coupled GCM. *Mon. Wea. Rev.*, **135**, 2700–2715, https://doi.org/10.1175/MWR3415.1.

Waliser, D., and Coauthors, 2009: MJO simulation diagnostics. *J. Climate*, **22**, 3006–3030, https://doi.org/10.1175/2008JCLI2731.1.

Wang, B., and H. Rui, 1990: Synoptic climatology of transient tropical intraseasonal convection anomalies: 1975-1985. *Meteor. Atmos. Phys.*, **44**, 43–61, https://doi.org/10.1007/BF01026810.

Wang, L., T. Li, E. Maloney, and B. Wang, 2017: Fundamental causes of propagating and nonpropagating MJOs in MJOTF/GASS models. *J. Climate*, **30**, 3743–3769, https://doi.org/10.1175/JCLI-D-16-0765.1.

——, ——, ——, and T. Nasuno, 2018: Impact of Rossby and Kelvin wave components on MJO eastward propagation. *J. Climate*, **31**, 6913–6931, https://doi.org/10.1175/JCLI-D-17-0749.1.

Wu, C. H., and H. H. Hsu, 2009: Topographic influence on the MJO in the Maritime Continent. *J. Climate*, **22**, 5433–5448, https://doi.org/10.1175/2009JCLI2825.1.

Yoo, C., S. Park, D. Kim, J. H. Yoon, and H. M. Kim, 2015: Boreal winter MJO teleconnection in the Community Atmosphere Model version 5 with the unified convection parameterization. *J. Climate*, **28**, 8135–8150, https://doi.org/10.1175/JCLI-D-15-0022.1.

Zhang, C., 2005: Madden–Julian Oscillation. *Rev. Geophys.*, **43**, RG2003, https://doi.org/10.1029/2004RG000158.

——, 2013: Madden–Julian oscillation: Bridging weather and climate. *Bull. Amer. Meteor. Soc.*, **94**, 1849–1870, https://doi.org/10.1175/BAMS-D-12-00026.1.

——, and J. Ling, 2017: Barrier effect of the Indo-Pacific Maritime Continent on the MJO: Perspectives from tracking MJO precipitation. *J. Climate*, **30**, 3439–3459, https://doi.org/10.1175/JCLI-D-16-0614.1.

Zhang, G. J., and N. A. McFarlane, 1995: Sensitivity of climate simulations to the parameterization of cumulus convection in the CCC-GCM. *Atmos.–Ocean*, **3**, 407–446, https://doi.org/10.1080/07055900.1995.9649539.